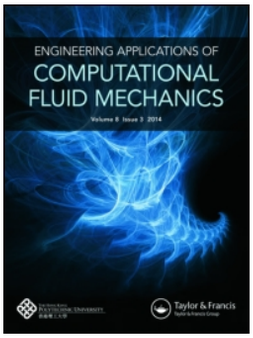

Engineering Applications of Computational Fluid Mechanics

ISSN: 1994-2060 (Print) 1997-003X (Online) Journal homepage: https://www.tandfonline.com/loi/tcfm20

Numerical investigation of the effect of leakage flow through erosion-induced clearance gaps of guide vanes on the performance of Francis turbines

Sailesh Chitrakar, Ole Gunnar Dahlhaug & Hari Prasad Neopane

To cite this article: Sailesh Chitrakar, Ole Gunnar Dahlhaug & Hari Prasad Neopane (2018) Numerical investigation of the effect of leakage flow through erosion-induced clearance gaps of guide vanes on the performance of Francis turbines, Engineering Applications of Computational Fluid Mechanics, 12:1, 662-678, DOI: 10.1080/19942060.2018.1509806

To link to this article: https://doi.org/10.1080/19942060.2018.1509806

© 2018 The Author(s). Published by Informa UK Limited, trading as Taylor & Francis Group

Published online: 30 Aug 2018.

Submit your article to this journal

Article views: 704

View related articles

View Crossmark data

Citing articles: 1 View citing articles

Full Terms & Conditions of access and use can be found at
https://www.tandfonline.com/action/journalInformation?journalCode=tcfm20

ENGINEERING APPLICATIONS OF COMPUTATIONAL FLUID MECHANICS
2018, VOL. 12, NO. 1, 662–678
https://doi.org/10.1080/19942060.2018.1509806

Taylor & Francis
Taylor & Francis Group

OPEN ACCESS Check for updates

Numerical investigation of the effect of leakage flow through erosion-induced clearance gaps of guide vanes on the performance of Francis turbines

Sailesh Chitrakar[a], Ole Gunnar Dahlhaug[b] and Hari Prasad Neopane[a]

[a]Department of Mechanical Engineering, Kathmandu University, Dhulikhel, Nepal; [b]Department of Energy and Process Engineering, Norwegian University of Science and Technology, Trondheim, Norway

ABSTRACT

Abrasive wear in the clearance gap of guide vanes (GVs) increases the gap size, which deteriorates the flow and causes loss of efficiency. This paper investigates the performance of a Francis turbine including erosion-induced clearance gaps on the GVs. The effect of the gap on the performance of the turbine is studied numerically, by using the GV and runner blade passages. The results are compared with an experiment conducted in a single GV rig, developed for the same model. Simulations are performed for GVs with NACA0012, NACA2412 and NACA4412 profiles with each at 11 operating conditions. It is found that the clearance gap induces a leakage flow due to the pressure difference between adjacent sides. The leakage flow mixes with the main flow, forming a vortex filament, which is driven inside the runner. By using an example of a power plant in Nepal affected by sediment erosion, it is found that these vortices containing sediment particles erode the inlet of the runner blade towards hub and shroud. Comparison between the three NACA profiles shows that NACA0012, which is the current shape of GV in the plant, causes a maximum loss due to the leakage flow. The asymmetrical profiles contrarily are found to increase the efficiency of the turbine at all operating conditions. Such profiles are also inferred to have the minimum influence of erosion and pressure pulsations problems at runner inlet. In short, this paper gives an overview of the potential effect of the eroded GV on the turbine's performance and compares different GV profiles to minimize such effects.

ARTICLE HISTORY
Received 30 April 2018
Accepted 5 August 2018

KEYWORDS
Francis turbine; erosion; leakage flow; clearance gap; CFD; guide vane

Nomenclature

GV	Guide Vane
NACA	National Advisory Committee for Aeronautics
PIV	Particle Image Velocimetry
CFD	Computational Fluid Dynamics
MW	Mega Watt
kW-h	kilo Watt – hour
ppm	parts per million
BEP	Best Efficiency Point
GCI	Grid Convergence Index
LE	Leading Edge
TE	Trailing Edge
L_{ff}	Leakage flow factor (-)
Φ	variable for GCI calculation
r	grid refinement factor (-)
e_a	approximate relative error (-)
e_{ext}	extrapolated relative error (-)
α	stagnation angle (degree)
H	net head (m)
C_u	tangential velocity component (m/s)
V_o	reference velocity (m/s)
V_y	velocity component normal to the chord (m)
P^*	fluctuating pressure (-)
$\bar{P}$	mean pressure (Pa)

1. Introduction

Clearance Gap in guide vanes (GV) of Francis turbines adds to the total loss due to the formation of the secondary flow inside the gap. It was studied that the size of the clearance gap of up to 0.5 mm (in 97 mm GV height) can be allowed without causing significant losses in low specific speed turbines (Thapa, Dahlhaug, & Thapa, 2017). However, deflection of head cover due to water pressure and continuous wear of the surface increases the size of the gap. Figure 1 shows the results of thermodynamic efficiency test conducted at Lio Power Plant (Power = 45 MW and Head = 335 m) for different size of the GV's clearance gap (Brekke, 1988). The height of the original GV was 230 mm. It can be seen that by increasing the clearance gap by 1 mm, the efficiency drops by about 2%.

CONTACT Hari Prasad Neopane hari@ku.edu.np

© 2018 The Author(s). Published by Informa UK Limited, trading as Taylor & Francis Group.
This is an Open Access article distributed under the terms of the Creative Commons Attribution License (http://creativecommons.org/licenses/by/4.0/), which permits unrestricted use, distribution, and reproduction in any medium, provided the original work is properly cited.

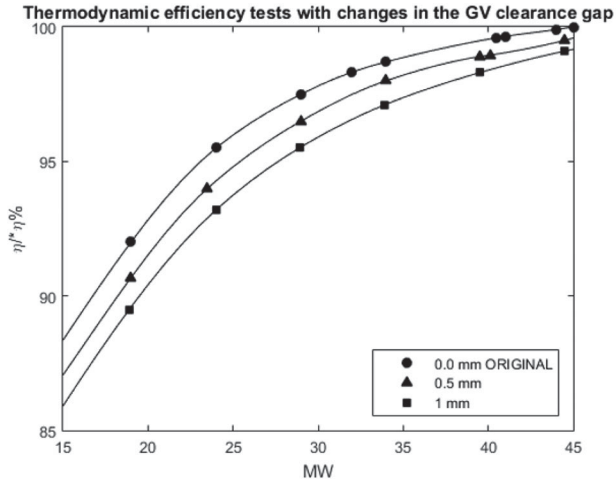

Figure 1. Efficiency of turbines at Lio Power Plant with clearance gap of 0 mm, 0.5 mm and 1 mm (Brekke, 1988).

The use of numerical techniques such as CFD is being widely used in many engineering applications (Fotovatikhah et al., 2018, Mou, He, Zhao, & Chau, 2017). The study of leakage flow through the clearance gap of the blades of turbines is found to have been studied for both compressible and incompressible flows. A numerical simulation was carried out to study the tip-leakage flow from the rotor tip region of an aero-engine (Zuojun, Weiyang, Peijie, Pingping, & Lei, 2014). Figure 2(a) shows the total pressure loss coefficient (Y_P) at the exit plant of the rotor. The tip-leakage vortex is seen as circular contours having the maximum loss. Similarly, a detailed flow physics of the tip-leakage flow and vortex was studied in a linear turbine cascade using CFD (Tallman & Lakshminarayana, 2001). The characteristics of the leakage flow based on their position were categorized, as shown in Figure 2(b). It was shown that the passage flow and leakage jet shear across each other, creating a helical type of roll-up.

Whereas Figure 2 shows the results of rotating blades in compressible flows, the tip vortex due to rotating vanes in hydro-turbines is mainly studied in Kaplan turbines (Mulu, Cervantes, Devals, Vu, & Guibault, 2015). In the case of Francis turbines, both stay vane and runner blades are attached to the hub and shroud in a fixed position. However, to enable opening and closing of GVs, a shaft is connected between GVs and a regulating ring, which makes all the GVs rotate with the same angle. A small clearance gap or a dry clearance (0.05–0.1 mm) is present on each side of GV to allow free rotating movement without friction. Besides the adjustment of the discharge and angular momentum at the runner inlet, the shape of the GVs is also designed to convert static head of the water into velocity head. It has been reported that the pressure drop across the GVs is approximately 40% of the net head at full load and 50% of the net head at small GV opening (Brekke, 2002) as shown in Figure 3. This creates the highest acceleration of the flow within the region, making the flow highly unsteady. In GVs containing clearance gap of a significant size, the flow is aggravated, which is carried downstream to reduce the turbine's performance.

A study similar to Figure 2(b) was conducted in a single GV rig of a Francis turbine (Chitrakar, Thapa, Dahlhaug, & Neopane, 2016). The leakage flow was categorized into four types, as shown in Figure 4. The first category is the flow in the suction side, which does not directly contribute to the leakage flow, but combines with them to form the passage vortex. Another category of flow enters the leading edge and starts diverting from the GV after traveling around 30% of the chord length. The

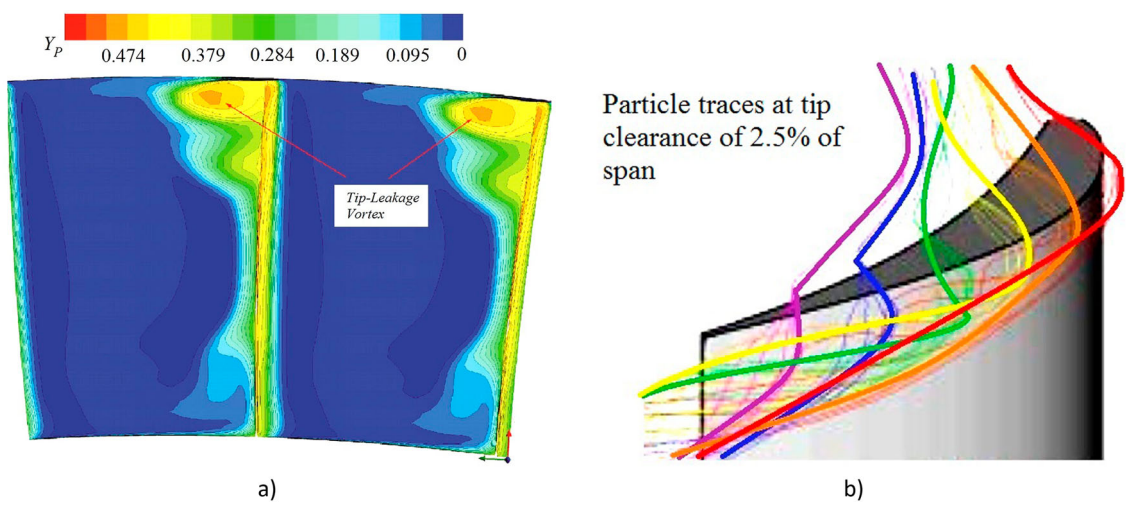

Figure 2. (a) Total pressure loss coefficient at the exit plane of a rotor blade (Zuojun et al., 2014) (b) Leakage flow through the clearance gap of height 2.5% of the span (Adapted from Tallman & Lakshminarayana, 2001).

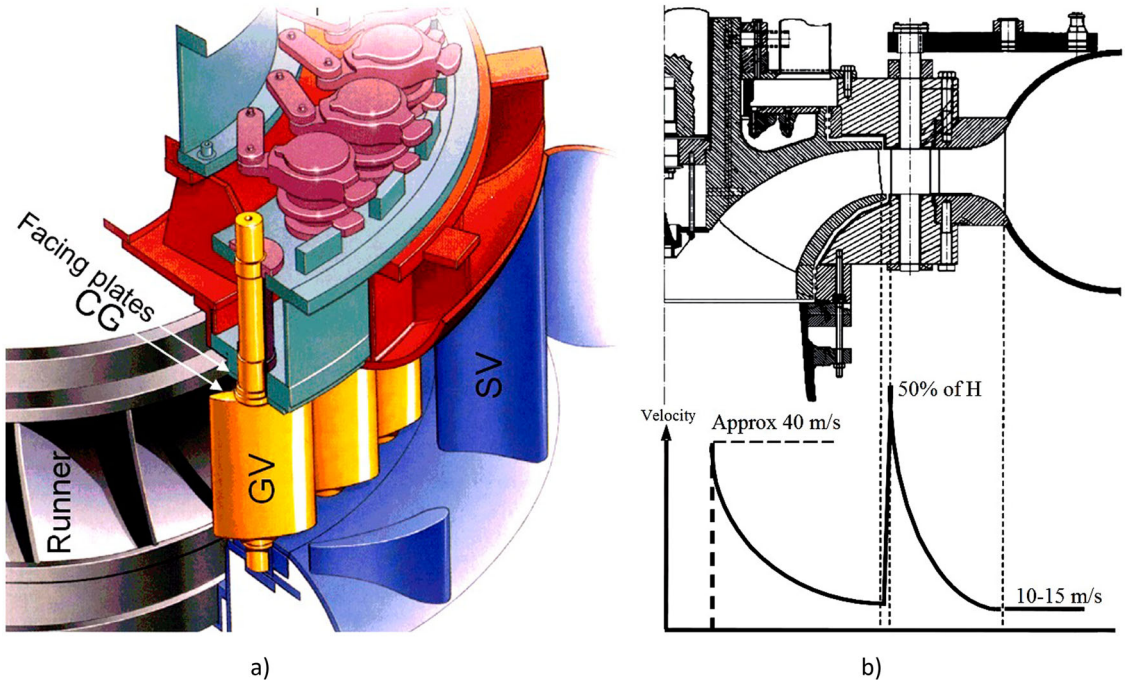

Figure 3. (a) Sectional 3D view of a Francis turbine and (b) velocity distribution inside Francis turbine (Thapa, Dahlhaug, & Thapa, 2015).

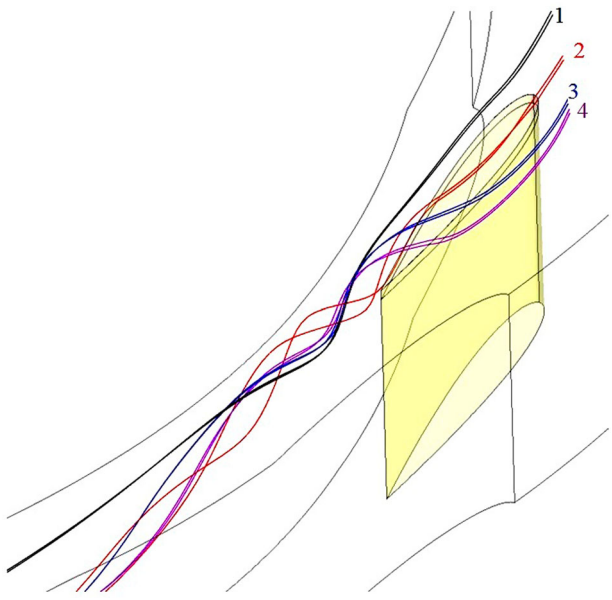

Figure 4. Types of leakage flow in GV of Francis turbine obtained from CFD in a single GV rig (Chitrakar, Thapa, Dahlhaug, & Neopane, 2017).

third category enters the clearance gap from pressure side due to the pressure difference between the two sides of the GV. The fourth category is the flow below the clearance gap, which is entrained by the high pressure gradient along the span.

A CFD-based simulation was also carried out to study the effect of the leakage flow in GVs due to head cover deflection induced by water pressure (Eide, 2004). This study showed that the increase in the clearance gap influences the main flow, underlining the importance of minimizing the cover deflection. In another study (Patel, Jain, Motwani, & Patel, 2013), numerical simulations were carried out using RANS equations with the standard $k-\varepsilon$ turbulence model under steady state conditions for a pump turbine. In this study, the opening angle of GVs using NACA-4418 profile was optimized. There are also some other research works which used numerical techniques to predict the characteristics and effects of the leakage flow through clearance gaps (Koirala, Zhu, & Neopane, 2016, Zhao, Billdal, Nielsen, & Brekke, 2012).

A single GV rig was developed to study the physics of the leakage flow inside the clearance gap of a GV with a height of 97 mm (Thapa, Trivedi, & Dahlhaug, 2016). The rig is able to produce flow fields around the GV similar to the real turbine. The velocity in this region was measured using a Particle Image Velocimetry (PIV) technique. Although the measurements were taken in a 2D plane, the vortex moving out of the plane could be predicted by measuring at several span positions (Thapa et al., 2017). The vortex was seen to originate from leakage flow, with a tendency to move away from the wall while traveling downstream (Chitrakar, Thapa, et al., 2017). Figure 5 explains a concept of leakage flow through clearance gaps on a GV cascade. The leakage flow mixes with the flow in the suction side forming a vortex. The figure shows vortex cores at the plane of the runner inlet.

The single GV rig was also used to test GVs with different profiles, both numerically (Chitrakar, Thapa,

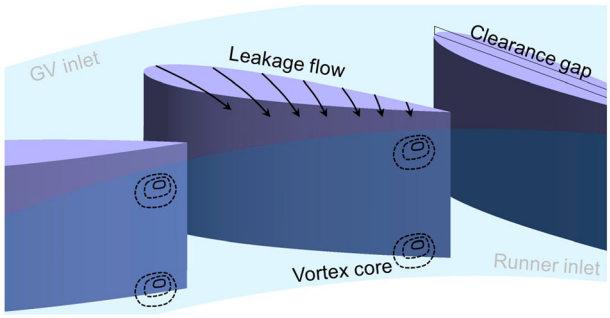

Figure 5. Concept of leakage flow through the clearance gap of GVs (Chitrakar, Neopane, & Dahlhaug, 2018).

et al., 2017) and experimentally (Chitrakar, Neopane, & Dahlhaug, 2017). It was seen that GVs with flatter suction side could minimize leakage flow by reducing the pressure difference between adjacent sides. However, the measurements were conducted at the designed opening angle. The rig was not suitable for testing at off-designed conditions because of the fixed walls located at the place of neighboring GVs. Besides, since the rig did not contain the runner, the effect of the vortices on the performances of the turbine could not be estimated.

This study focuses on the consequences of leakage flow on the performances of the turbine. Since this study uses a numerical approach for testing, the result of GV rig is used to compare with the obtained results. The major objective is to investigate if the change in the GV profile can minimize the overall effect of an increase in the size of the clearance gap after erosion, at all operating conditions.

2. Scenario of sediment erosion in turbines

Erosive wear or erosion is a form of wear caused due to the impacts of solid or liquid particles on a solid surface. The abrasive wear or abrasion is another form, which has a similar wear mechanism compared to the erosive wear, but the angle of impingement is much lower than the erosive wear (Stachowiak & Batchelor, 2006). Francis turbine components exposed to hard sediment particles experience both erosion and abrasion type of wear. It is reported that out of 7×10^9 tons of suspended sediment carried to the ocean yearly from all rivers globally, about 70% is derived from southern Asia (Milliman & Meade, 1983). Due to excessive sediment and hard mineral contents in it, the turbines in the power plants under the Himalayan river faces operation challenges due to erosion (Thapa, 2004). Although the problem is predominant in South Asia, other parts of the world, such as Europe and South America are also continuously facing the consequences of sediments (Felix, Albayrak, Abgottspon, & Boes, 2016). In one of the power plants in Switzerland (1×2.6 MW Pelton turbine and 7×0.4 MW Girard turbines), the efficiency dropped by about 4% during only six days of sediment season. In a power plant in Northern India (1×130 MW Francis turbine), the turbines are maintained every year due to the sediment concentration of 500 to 600 ppm in its river (Masoodi & Harmain, 2017). In the same power plant, the average erosion rate of 4.5 mm/year was measured in the runner blades. An economic impact analysis due to sediment erosion was calculated from a power plant in Colombia (10 MW Francis turbine), which showed a total loss (including efficiency loss, material loss, repair and management) of more than 12 million US Dollars per year for the electricity value of 0.17 US Dollars per KW-h (Teran et al., 2016).

It has been seen through literatures that erosion of turbines eventually leads to the loss of efficiency. In Jhimruk HPP (3×4.1 MW), the hydraulic efficiency of the turbine decreased by around 5%, after severe erosion during a monsoon season (Dahlhaug, Skåre, Mossing, & Gutierrez, 2010). In Maneri Bhali Stage II (4×76 MW) (Singh, Banerjee, Patel, & Tiwari, 2013), the efficiency of one of the units decreased by 2.4% at full load and by 4.9% at 50% load after erosion. In Kaligandaki HPP (3×48 MW), the size of the clearance gaps were measured in one of the units (Koirala, Thapa, Neopane, Zhu, & Chhetry, 2016). Towards leading edge, the average clearance gap was found to be 2.5 mm after 16,500 h of operation, compared to the designed clearance gap of 0.6 mm. Towards trailing edge, the average increment was found to be 4.2 mm after 16,500 h of operation. This shows that the pressure difference towards the trailing edge is higher than the leading edge, which results in high velocity of particles, causing more erosion in these regions.

This study uses the case of Jhimruk HPP, located in Nepal. It is a run-of-river type power plant operating at a net head of 201.5 m and designed discharge of 2.35 m^3/s. There are three units of horizontal Francis turbines running at 1000 rpm. The plant is facing severe operational and maintenance issues due to excessive sediments in its river. Apart from excessive sediments, the percentage of quartz in a sediment sample taken from this power plant was found to be between 60% and 70% (Thapa, 2004). Figure 6(a) shows erosion at one end of GVs. More erosion was found towards the second half of the chord, after shaft. One reason for such erosion is the high turbulence behind the shaft due to separation of flow through the cylindrical shaft. Another reason is the abrasion from the particles due to cross-flow or leakage flow inside the gap from one side to another. It has been found that the pressure difference between the adjacent sides of the GVs directly influence the intensity of leakage

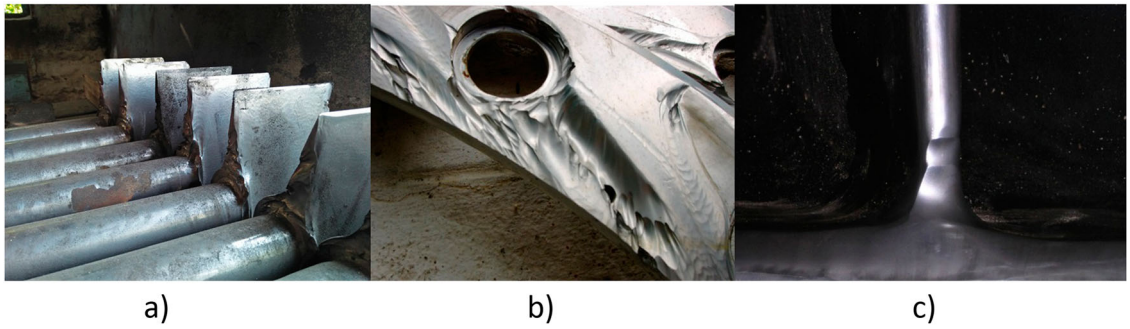

Figure 6. Erosion at (a) GV's facing ends, (b) facing plates and (c) runner blade inlet (Picture Courtesy: O.G. Dahlhaug).

flow and consequently, the abrasion (Chitrakar, Thapa, et al., 2017). Figure 6(b) gives a closer view of the erosion on facing plates. Horseshoe vortices are formed at corners between GVs and facing plates, forming eroded patterns in the shape of GV profile. Due to the opening and closing of GVs, the eroded patterns are formed throughout the range of GV's opening angles. More erosion occurs on its surface due to continuous leakage flow through the gap. The erosion at the ends of GVs and the facing plates eventually increases the gap size, which is also added by the deflection of the covers due to water pressure (Eide, 2004). Figure 6(c) shows closer view of the erosion at the inlet of the runner blade towards one of the edges. This erosion might have occurred due to the disturbances caused by the interaction of the leakage flow with the main flow. In some cases, cavitation might also occur because of the improper stagnation angle at these regions.

3. Hydrofoil shapes and clearance gap

This study compares the performance of three different NACA profiles. The reference profile is NACA0012, which is the current shape of GV in Jhimruk HPP. This shape of GV is symmetric along the chord and has the maximum thickness of 12% of the chord length at 30% chord. The reference shape is compared with NACA2412 and NACA4412, which have the same maximum thickness as NACA0012, but have camber of 2% and 4% respectively at 40% chord. The chord length of the GV is equal to 140 mm. The inclusion of clearance gaps in this study represents the eroded region. As shown in Figure 7, it is assumed that the original width of the clearance gap is t. After erosion, the width of the clearance gap increases to $t + \Delta t$. The actual eroded surfaces are non-uniform, as shown in Figure 6. The eroded pattern causes more instability in the flow, which adds to the losses in the turbine. The pattern of erosion in a blade varies according to the age of the blade and operating conditions of the turbine. It is, therefore, assumed that the surface of the eroded region is uniform to get a general picture of the leakage flow through GVs. The clearance gap widths of 0.5, 1, 1.5 and 2 mm were tested in this study.

The opening angles of the GV mentioned in this study represent angles with respect to best efficiency point (BEP). Hence, the GV angle at BEP is 0°, which corresponds to the designed flow of 2.35 m^3/s, or 100% flow. In the case of part load conditions, the GV opening angle reduces, which has been represented as −1°, −2° and so on. The flow in this case was reduced depending upon the operational flow. Similarly, in the case of higher load, the GV opening angle increases, which has been represented as 1°, 2° and so on.

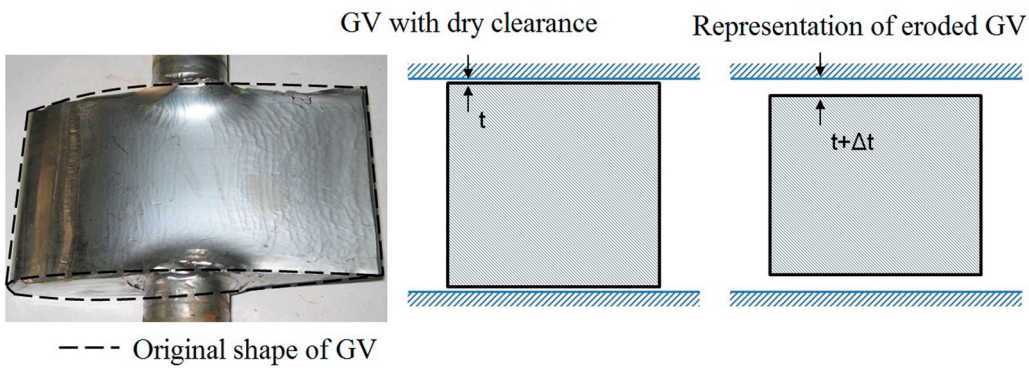

Figure 7. Representation of the eroded GV as change in the size of the clearance gap.

4. Numerical model

This study primarily uses numerical analysis to study the flow field inside the Francis turbine. ANSYS CFX is used to conduct CFD simulations in a region of the turbine. Simulations were carried out for 3 GV profiles and 11 opening angles including BEP. Hence, 33 different combinations were tested in the steady analysis. The domain for the steady analysis consists of 4 GVs and 3 runner blade passages, as shown in Figure 8. The full model of the turbine consists of 24 GVs and 17 runner blades. The dimension of the turbine and design of these blades correspond to the actual turbine in Jhimruk HPP excluding splitters. The domain was divided into 3 sub domains, GV (stationary), runner (rotating) and a portion of the draft tube (stationary). At the inlet, a mass flow rate corresponding to the designed flow of the turbine was given for BEP. This flow varied according to different GV openings, maintaining almost constant head for all the cases. Atmospheric pressure was assumed at the outlet of the draft tube for all the cases. The objectives of steady analyses were to (i) study the overall performance of the turbine at all operating conditions and (ii) study the leakage flow through the clearance gap, for 3 NACA profiles of GV discussed in Section 3.

The instantaneous continuity and Navier–Stokes equations form a set of four equations with four unknowns, velocity in all directions (u, v, w) and pressure (p). These equations are highly non-linear partial derivative equations, which requires computational methods to solve. In this study, Reynolds averaging method is used,

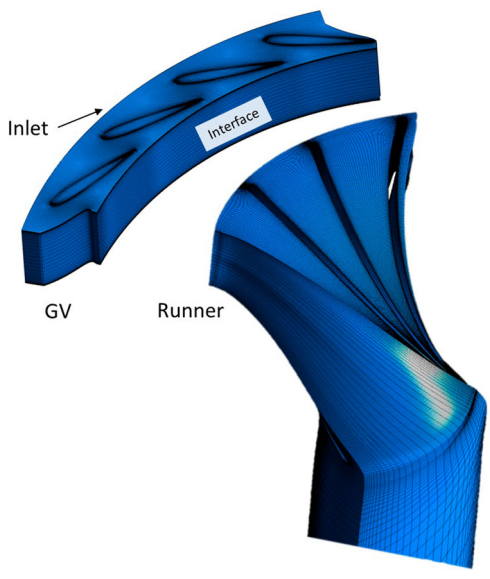

Figure 8. GV and runner domains for steady CFD analysis and the mesh used in the simulations with the total mesh count of 2.82 M in four GV and 1.2 M mesh in three runner blade passages.

which divides a variable, u_i into averaging component, $\overline{u_i}$, and a fluctuating component u_i'. The substitution of these terms results in the following equations:

$$\frac{\partial \bar{u}_i}{\partial x_i} = 0 \tag{1}$$

$$\frac{\partial \bar{u}_i}{\partial t} + \bar{u}_j \frac{\partial \bar{u}_i}{\partial x_j} = -\frac{1}{\rho}\frac{\partial \bar{p}}{\partial x_i} + \frac{\partial}{\partial x_j}\left(\nu \frac{\partial \bar{u}_i}{\partial x_j} - \overline{u'_i u'_j}\right) \tag{2}$$

where, $\overline{u_i}$ is the time-averaged velocity components, $\overline{p}$ is the time-averaged pressure, ρ is the fluid density, ν is the fluid kinematic viscosity, u_i' is the fluctuating velocity components and t is the time

The Reynolds' averaging maintains the continuity equation, but results in additional terms, Reynolds' stresses in the time-averaged momentum equations, which are calculated using different turbulence models.

The turbulence model, in general, can be classified into classical models and large eddy simulations (Vergteed & Malalasekera, 1995). Classical models use Reynolds time-averaged equations, which can be divided into eddy viscosity models and Reynolds stress models. For an incompressible flow, in the eddy viscosity model, the Reynolds stresses are linked to mean rates of deformation using Boussinesq's hypothesis:

$$\tau_{ij} = -\rho \overline{u'_i u'_j} = \mu_t \left(\frac{\partial \bar{u}_i}{\partial x_j} + \frac{\partial \bar{u}_j}{\partial x_i}\right) \tag{3}$$

where μ_t is the eddy viscosity (Pa s). The kinematic turbulent or eddy viscosity is denoted by $\nu_t = \mu_t/\rho$, with dimensions m^2/s.

The velocity and turbulent length scale are solved using two separate transport equations in the case of two-equation eddy viscosity turbulence models, one for kinetic energy, k and one for turbulent dissipation rate, ε, or the specific dissipation rate, ω. In one of the two-equation models, $k-\varepsilon$, the turbulence viscosity,ν_t is related to the turbulence kinetic energy, k and the dissipation rate, ε by the relation:

$$\nu_t = C_\mu \frac{k^2}{\varepsilon} \tag{4}$$

where C_μ is the constant (Durbin & Reif, 2001)

$k-\varepsilon$ turbulence model and RNG $k-\varepsilon$ model, which is based on the renormalization group analysis of the Navier–Stokes equations are found to be used widely in the simulations of Francis turbines (Lewis & Cimbala, 2015). However, some studies have pointed out the limitations of $k-\varepsilon$ model, especially in the regions near the wall (Durbin & Reif, 2001). Wilcox model or $k-\omega$ model is more accurate than $k-\varepsilon$ model in the near-wall boundary layer. However, $k-\omega$ model is strongly

sensitive outside the boundary layer (Wilcox, 1993). The limitations of $k-\varepsilon$ and $k-\omega$ model were overcome by using shear stress transport (SST) model, which uses blending function to ensure a proper selection of $k-\varepsilon$ and $k-\omega$ model. A review on numerical techniques applied to hydraulic turbines showed that the CFD results using SST turbulence model in the case of Francis turbines showed good agreement with experiments (Trivedi, Cervantes, & Dahlhaug, 2016). A sensitivity study of different turbulence model was performed for the CFD of one GV with Reynolds' number of 1.52E + 07 containing 2 mm clearance gap (Chitrakar, Thapa, Dahlhaug, & Neopane, 2016). This study showed that SST turbulence model is one of the suitable models for this application. Hence, the simulations in this study used the SST turbulence model, with high-resolution discretization in the advection scheme and first order upwind scheme in the turbulence equations.

Although steady analyses were performed for 33 different combinations, transient analyses were carried out only for 9 combinations, which included 3 operating conditions for each GV profile. These operating conditions corresponded to −5°, 0° and 5° GV opening angles compared to BEP. In this case, the domain consists of the full model of the turbine, so that the interface ratio of 1 is maintained between stationary and rotating components. The transient simulations were carried out for total time corresponding to 1.5 revolutions, and at a time step of 1° per step. For a reference case, a time step dependency test was performed by using the time steps of 0.5° 1° and 1.5° per step. The variation of the maximum pressure amplitude at mid-span between the time steps of 0.5° and 1° was found to be less than 0.1%. The objectives of transient analyses were to (i) predict the true transient interaction of the flow between GV and runner, (ii) calculate the pressure pulsation at the runner inlet for 3 GV profiles. The boundary conditions for respective opening angles were maintained same as the steady analysis.

4.1. Mesh sensitivity

The model of the turbine's runner blade and GV were in the form of co-ordinates at different span height of the vane. These co-ordinates were exported in the curve format (.curve), which is a standard format that can be imported in ANSYS Turbogrid for generating mesh. The curve file consists of the points classified on different spans of the vane. The reference GV consisted of symmetrical NACA0012 profile, which was compared with NACA2412 and NACA4412 in this study. The model of GV and runner was discretized separately using hexahedral structured mesh, as shown in Figure 8. The discretization error was calculated using the GCI method (Celik et al., 2008). The mesh refinement was done by increasing the distribution of mesh in each direction, i.e. implementing the grid refinement factor (r) of 1.3X. The mesh sensitivity study was carried out by taking one GV and one runner blade passages. The GVs contained a clearance gap of 1 mm at both sides. For three sizes of the mesh, the clearance gap contained 5, 7 and 9 elements along the height, with total mesh count of 0.39 M, 1.03 M and 2.82 M, respectively. Pressure difference (ΔP) between the pressure and suction sides of the GV and hydraulic efficiency of the turbine were chosen as the monitored variables. The calculation of the uncertainties involved due to mesh size was done using the reference (Celik et al., 2008).

Table 1 shows the uncertainty and extrapolated values of the efficiency measured. In the table, $\Phi_{\text{coarse}(3)}$, $\Phi_{\text{medium}(2)}$, $\Phi_{\text{fine}(1)}$ and Φ_{ext} are the efficiencies obtained from coarse, medium and fine mesh, respectively. The table also shows the description and formula of various parameters used in the calculation. e_a^{21} and e_{ext}^{21} are the approximate and extrapolated relative errors. $\text{GCI}_{\text{fine}}^{21}$ signifies the grid convergence index, which is the numerical uncertainty associated with the fine mesh. The numerical uncertainty of the efficiency for the fine mesh was calculated to be 0.06%. This value was 0.14% for the medium mesh.

Figure 9 shows the uncertainties and extrapolated values of the pressure difference between pressure and suction sides at mid-span of GV. The discretization error bars are computed for the fine mesh. The numerical uncertainty for ΔP ranged from 0.5% to 26% with higher errors towards leading and trailing edges. However, size of the error bars around the mid-chord regions (x values in the graph: 0.5–0.7) seems to be larger than leading and trailing edges in the figure. This is because the pressure difference towards the mid-chord region is higher than the edges, which results in higher deviation of the calculated values. The final mesh contained over 2.82 M mesh elements in four GV passages and over 1.2 M mesh elements in three runner blade passages. The average value of $y+$ was ∼30 in all the near-wall regions and

Table 1. Discretization errors for the numerical solution.

Parameter	r_{21}	r_{32}	$\Phi_{\text{coarse}(3)}$	$\Phi_{\text{medium}(2)}$	$\Phi_{\text{fine}(1)}$	Φ_{ext}	e_a^{21}	e_{ext}^{21}	$\text{GCI}_{\text{fine}}^{21}$
Description	Grid refinement factors		Variables obtained from coarse, medium and fine mesh together with extrapolated values				$\left\lvert\frac{\varphi_1-\varphi_2}{\varphi_1}\right\rvert$	$\left\lvert\frac{\varphi_{\text{ext}}-\varphi_1}{\varphi_{\text{ext}}}\right\rvert$	$\frac{1.25\times e_a^{21}}{r_{21}-1}$
Values	1.3975	1.3829	94.37%	94.33%	94.31%	94.26%	0.00021	0.00054	**0.00068**

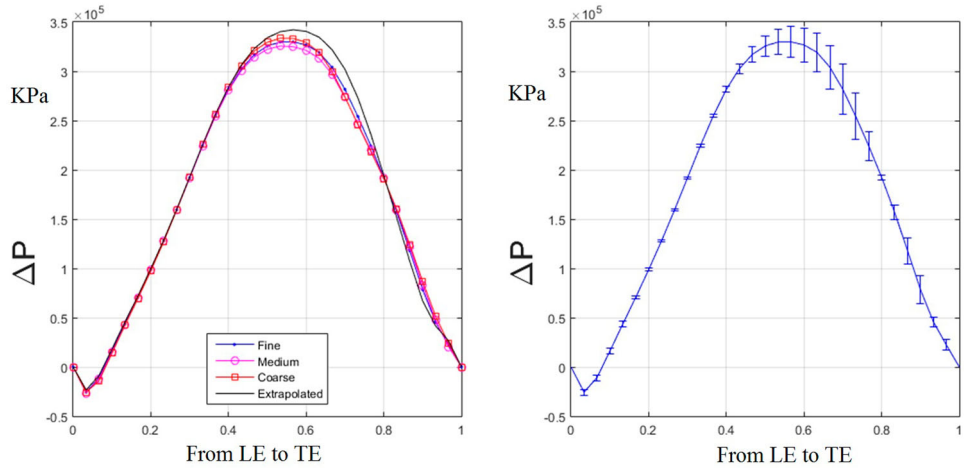

Figure 9. ΔP between pressure and suction side at mid-span with extrapolated values and discretization error bars.

~ 10 near the GV and runner blade boundaries. The runner and GV were connected using a frozen rotor mixing model in the case of steady simulations whereas transient rotor stator interface was used during the transient analyses.

5. Results and discussion

5.1. Comparison with experiment

The experiment was conducted in a single GV rig with the same dimensions as in the turbine simulated in this study. The rig was designed to match the velocity distribution around a single GV with the real turbine. The walls surrounding the rig were optimized to produce periodic velocity field between adjacent GVs, such that the real flow conditions are formed (Thapa et al., 2016). The total flow at the inlet of the rig was maintained at 1/12th of the total flow in the turbine, which corresponds to the actual flow in two GV passages (one passage at the upper side and one passage at the lower side of the GV). In a previous study (Chitrakar, Thapa, et al., 2017), both CFD and PIV were conducted in the GV rig to obtain the velocity field around GV. Figure 10 shows the velocity field at the mid-span obtained in the rig and in the turbine. With similar boundary conditions, it can be seen that the velocity distribution around the GV and the order of the magnitude of velocity are comparable between the two cases. Around the stagnation region, the velocity ranges between 10 and 14 m/s. The maximum velocity in the rig is around 35 m/s, which is in the region of lowest area downstream of GV. As the turbine does not contain this region, the maximum velocity remains close to 30 m/s. At the suction side, the velocity rises after the mid-chord position, signifying high pressure difference and consequent leakage flow through the gap. Although the rig and the turbine have a different flow domain, this comparison gave a basis for justifying the velocity trend around the GV obtained through numerical simulations in this study.

Whereas Figure 10 shows the velocity field obtained in the GV's mid-span, Figure 11 shows the velocity field inside the clearance gap obtained from both the single GV rig and simulations in the turbine. It can be seen from the figure that the leakage flow inside the clearance gap leads to acceleration of the flow after

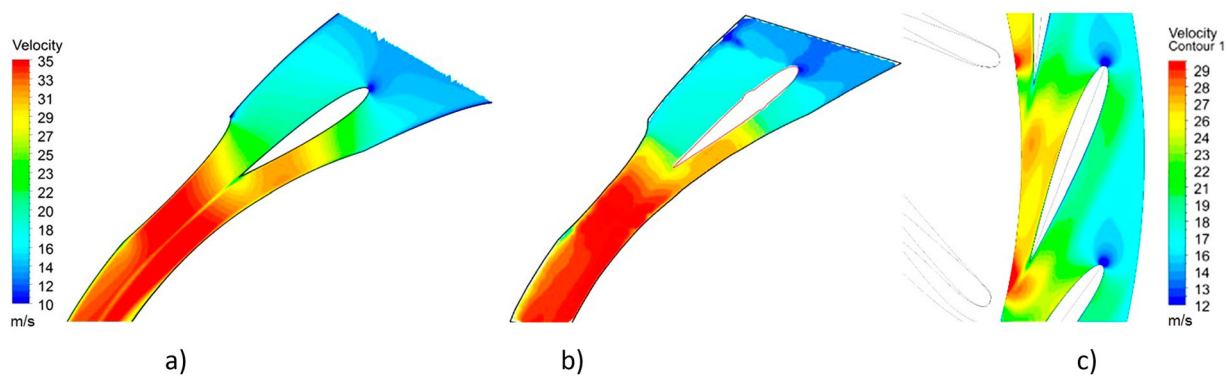

Figure 10. (a) CFD in single GV rig, (b) PIV in the rig with same velocity range and (c) CFD in turbine.

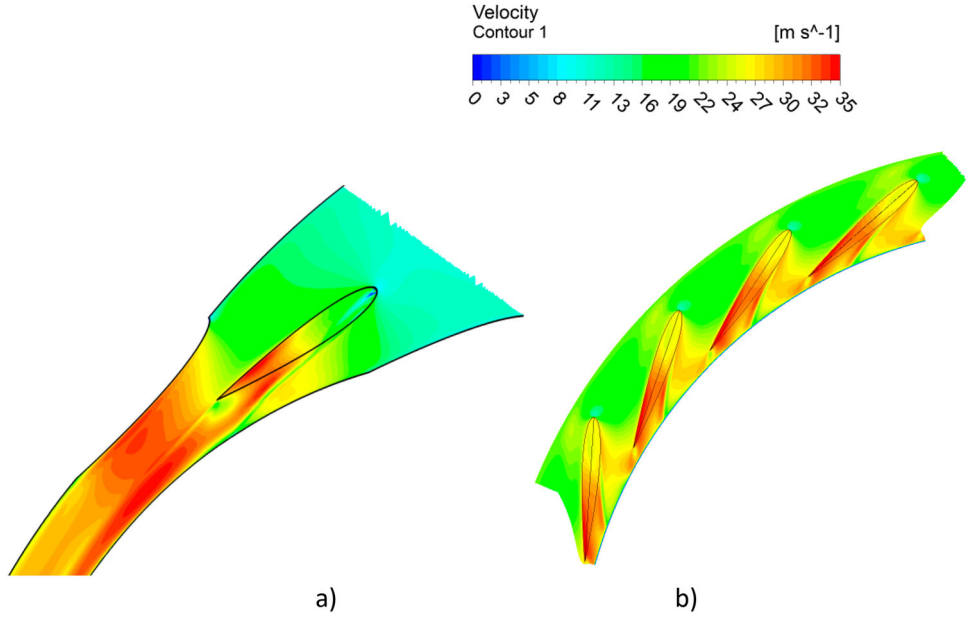

Figure 11. (a) Velocity field inside the clearance gap obtained in single GV rig (Chitrakar, Thapa et al., 2017) and (b) Velocity field inside the GV's clearance gap of the simulated turbine.

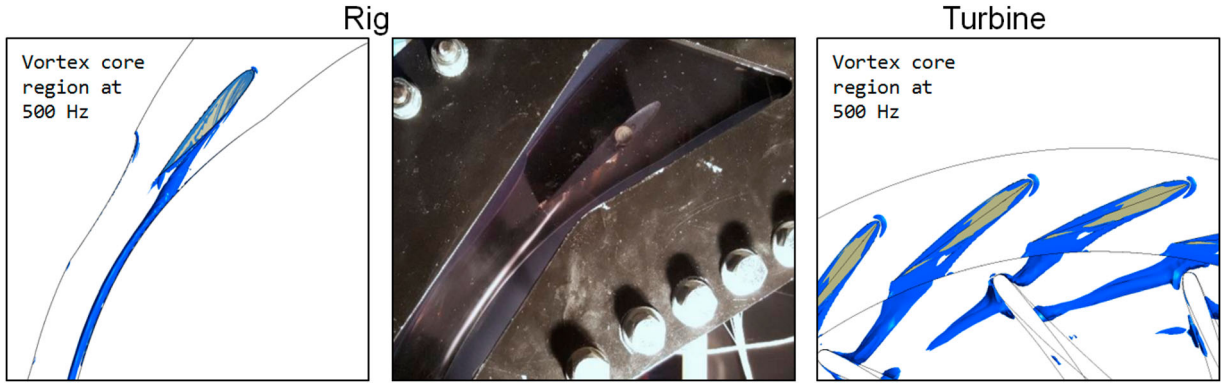

Figure 12. Vortex filament observed from the single GV rig and the turbine.

the mid-chord region, which causes flow disturbances towards the suction side of the GV. This velocity trend is followed by both the rig and the turbine. The simulations of the turbine performed in this study enable the understanding of how these vortices are hitting the runner blades and how it is affecting the overall performances of the turbine.

A vortex filament was observed during the experiment, originating towards the trailing edge and traveling downstream. The vortex was also observed from the CFD of the rig and the turbine. Figure 12 shows the comparison of the vortices between CFD and experiment in the rig and CFD in the turbine. The origin and path of the vortices in all the cases look similar. In the picture of the rig, the white line downstream of GV represents the vortex. Since the runner blade is close to the GV's trailing edge, the energy of the vortex is transferred to the inlet of the blade. Hence, the total length of the vortex filament in the turbine is less than in the rig. It was seen from these results that the GV rig developed for the same turbine providing equivalent boundary conditions produce similar velocity field and vortex. It has to be noted that these numerical and experimental studies were performed for the GV oriented at BEP. At this opening angle, the influence from the wall of the test rig is negligible because of the design method of the rig. Moreover, both the rig and the turbine contain same GV profile (NACA0012). Considering these aspects, further simulations in this study were carried out by using the same numerical model.

5.2. Effect of the size of the clearance gap

In this study, the clearance gap was considered to have a uniform surface. In a real condition, apart from the dry clearance gap, the eroded pattern is irregular as shown in Figure 6. The size of the clearance gap increases gradually

with continuous abrasion by the sediments. Since only one gap size is tested for further simulations, this section compares the effect of using different gap size. Stagnation angle at the inlet of the runner blade (α) at different span was taken as the parameter for comparison. The angle, α is described in Figure 14. The comparison was done at BEP, since other opening angles might influence the flow due to separation. The two GV profiles, NACA0012 and NACA4412 were tested. The size of the gap was varied from 0.5 to 2 mm at the interval of 0.5 mm. The gap influences the α angle near hub and shroud, as shown in Figure 13. The incidence angle reduces near the edges, which is proportional to the size of the gap. At 2 mm clearance gap, using NACA0012 profile, the stagnation angle (α) near hub and shroud reduces by 30%. It can also be seen that the angle is not affected significantly in NACA4412, compared to NACA0012 by increasing the gap. As the size of the gap influences the performance of the turbine linearly, the gap size of 1 mm was chosen for all the further simulations.

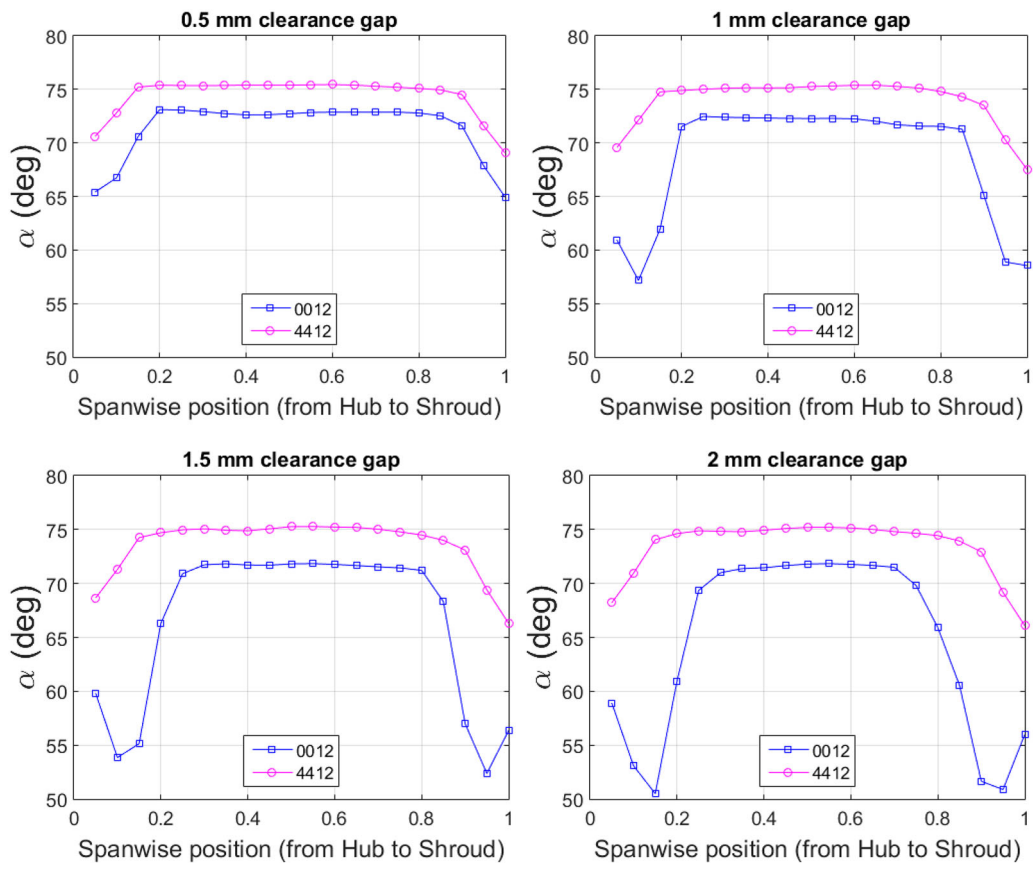

Figure 13. Stagnation angle at the inlet of the runner from hub (0) to shroud (1).

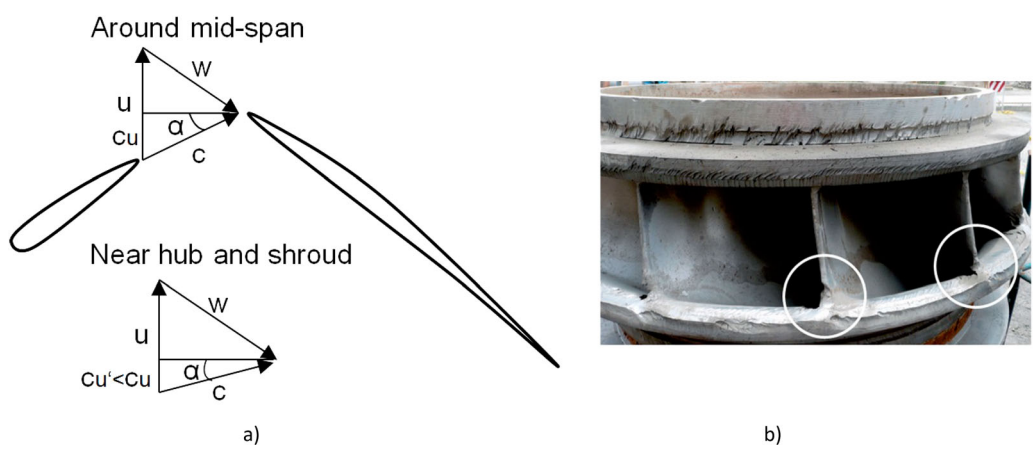

Figure 14. (a) Velocity triangle due to change in the stagnation angle and (b) potential effect of change in the stagnation angle.

Figure 14 shows the effect of the reduction of the incidence angle on the velocity triangle at the runner inlet. The reduction in the angle reduces tangential absolute velocity component (C_u) at the inlet of the runner. From Euler's equation of turbine, the hydraulic efficiency of the turbine is calculated as, $\eta_h = (u_1.C_{u1} - u_{2.}.C_{u2})/g.H$, with $C_{u2} = 0$ for BEP, the reduction of C_u at the inlet implies less efficiency. Improper stagnation angle might also enhance cavitation, because of a high pressure gradient between the two sides of the GV. A potential consequence is shown in the figure from Cahua HPP, where the inlet of the blade towards the shroud end experienced both erosion and cavitation (Dahlhaug et al., 2010).

5.3. Runner efficiency

Efficiency of the runner was calculated based on the available and extracted power of the runner. The extracted power was calculated from the torque generated in the rotating blades and the rotating speed of the turbine. The available power was derived from the discharge and the net head within the runner. Figure 15 is the plot of flow against efficiency at 1 mm clearance gap at both ends, where 100% flow implies BEP. The efficiency curves have a similar trend in all the three cases of GV profiles. The lowest efficiencies were found in part load conditions, when the flow is minimum. However, in all the operating conditions, it can be seen that the runner with GVs containing NACA4412 profile is most efficient. The rise in efficiency is in the range of 1.5–3%, compared to NACA0012. NACA2412 produces intermediate efficiencies, which is 0.5–1.5% more than NACA0012. The rise in efficiency can be related with the reduced leakage flow in asymmetric profiles. Comparison of the leakage flow is done in next sections. However, a fraction of the total efficiency rise might also be due to change in the GV outlet angle. This results in an increase in the stagnation angle at the inlet of the runner, as shown in Figure 13, which increases the swirl component, C_u.

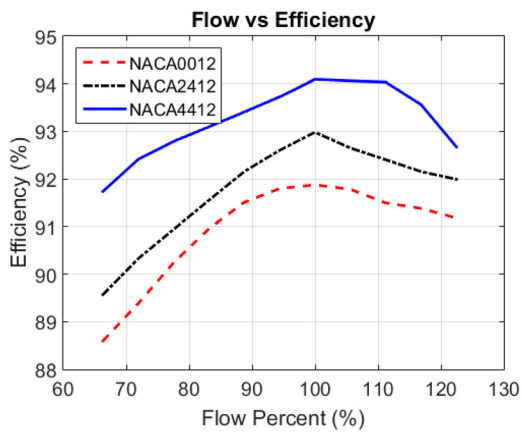

Figure 15. Efficiency of the runner at all operating points for 3 GV profiles.

5.4. Leakage flow at BEP

In this study, leakage flow is referred to the flow passed inside the clearance gap from high pressure to low pressure side of the GVs. The amount of leakage flow can be interpreted from the velocity vectors plotted inside the gap. Figure 16 shows the velocity vectors plotted along the chord (camber for the case of asymmetric profile) line inside the clearance gap for three hydrofoils. At BEP, the velocity vectors in NACA4412 follow the direction of the main flow. This is due to the similar pressure distribution around GV's adjacent sides. The velocity vectors in NACA0012 and NACA2412 seem to deviate away from the main flow significantly. This leakage flow mixes with the main flow to cause more disturbances in downstream turbine components.

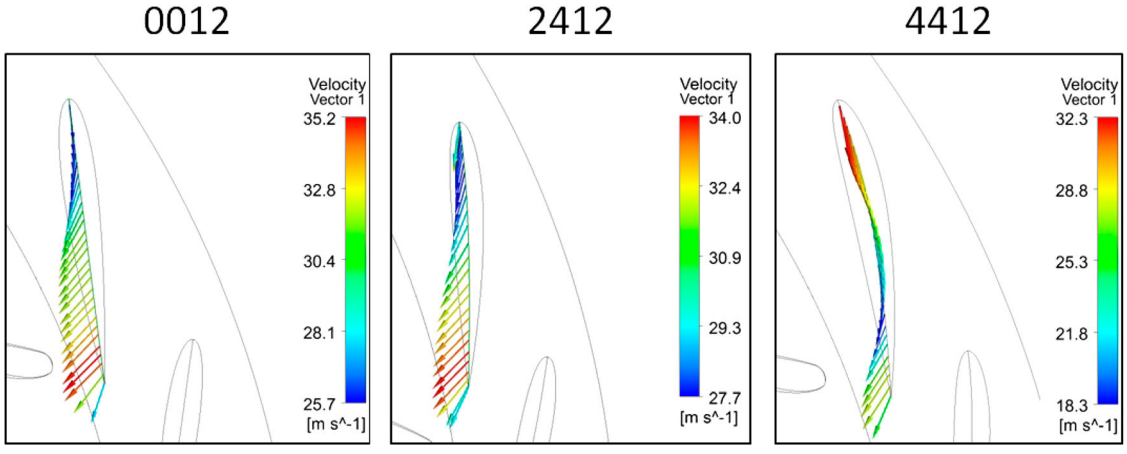

Figure 16. Velocity vectors along the camber line of the GVs at BEP.

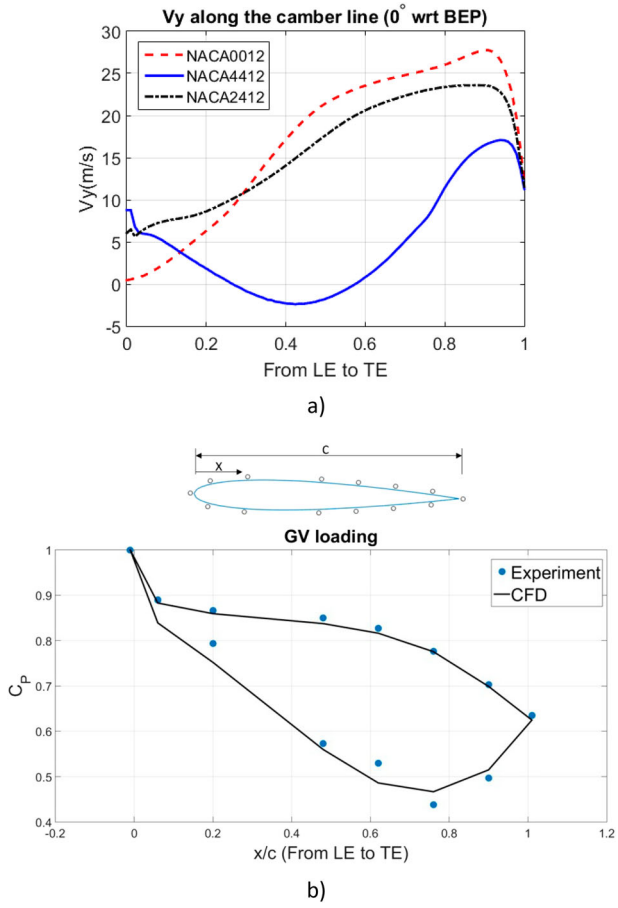

Figure 17. Velocity normal to camber line (V_y) from LE to TE and pressure distribution in single GV rig from a previous study (Chitrakar, Thapa, et al., 2017).

The velocity vectors shown in Figure 16 can be resolved in two components, one component following the path of the camber and another one, perpendicular to the camber line (V_y). In an ideal case, the flow follows the camber line, with $V_y = 0$ i.e. no leakage flow. Depending upon the velocity vector, V_y can be positive as well as negative, with larger values signifying more leakages. In Figure 17, the V_y component is plotted against the camber line, from leading edge (LE) to the trailing edge (TE) of the GV in the mid-plane of the clearance gap. In all the three cases, it can be seen that V_y is high towards the trailing edge of the GV, which can also be seen in Figure 16. Compared to NACA0012, the trend of V_y in NACA2412 is similar, with the maximum value dropping by around 20%. In the case of NACA4412, this drop is more than 40%. Also, in most of the locations, the value of V_y is close to zero. This result was compared with pressure distribution (Cp) around GV in single GV rig (Chitrakar, Thapa, et al., 2017). Figure 17 also shows the pressure distribution around NACA0012 profile at BEP condition, measured by CFD and experiment. Comparing this plot with V_y for NACA0012 shows a close relation between the two results. The pressure difference near the leading edge is close to zero, which signifies minimum cross-leakage flow. The pressure difference gradually rises as the flow moves along the GV, increasing the V_y component. Finally, near the trailing edge, the V_y component decreases again, due to the low pressure difference.

Figure 18 shows the iso-surface of the swirling strength at BEP obtained from transient analysis for three profiles. It is one of the methods to visualize the vortex, which represents imaginary part of complex eigenvalues of the velocity gradient tensor. The positive value of the discriminant of the velocity gradient tensor for complex eigenvalues gives positive swirling strength, indicating existence of swirling motion around local centers. The three GV profiles are compared at same swirling strength and velocity on the vortex core to justify the comparison. The iso-surfaces are extracted for $t = 0.075$ s. It can be seen that the strength of the vortices and velocity of the

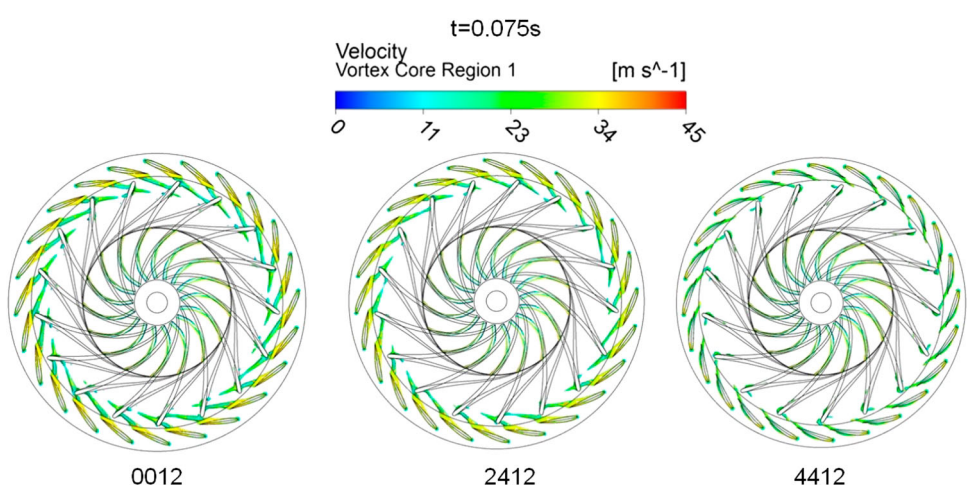

Figure 18. Iso-surface contours of swirling strength, s (500 1/s) with velocity.

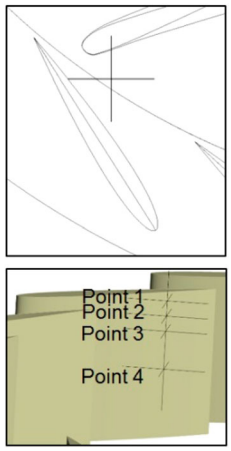

Figure 19. Points for measurement of pressure pulsations.

flow in NACA0012 is highest among the three profiles. This result can be related to Figures 16 and 17.

Unsteady pressure at four span position of the runner inlet was investigated. These positions are shown in Figure 19. Point 1 is inside the clearance gap plane, whereas Point 4 lies in the GV's mid-span plane. Figure 20 shows the pressure signal at BEP for three shapes of GV in four locations. The fluctuating pressure (P^*) (Trivedi, Cervantes, & Gandhi, 2016) was calculated by subtracting the mean pressure ($\bar{P}$) from the instantaneous pressure (P) and normalized by the reference pressure $(\rho E)_{BEP}$.

$$P^* = \frac{P - \bar{P}}{(\rho.E)_{BEP}}[-] \tag{5}$$

The instantaneous time (t^*) in Figure 20 was normalized by the total time step. It can be seen that the pressure fluctuation in Point 1 is affected by the vortex filament originated from the leakage flow, as there are two peaks at each blade passing frequency. Comparing it with the pressure fluctuation in Point 4, the additional peak is not seen due to minimal or no effect of the leakage flow towards the mid-span of the GV.

Figure 21 shows the Fourier-transformed pressure pulsation for three GV profiles at the located points with a sampling frequency of 6000 Hz. The first peak in the figure represents the blade passing frequency, which in this case is 400 Hz. The pulsating pressure exists in all the tested profiles. However, it can be seen that the magnitude in NACA4412 is the least among them. The value of the maximum pressure amplitude at Point 1 in NACA2412 reduces by 44.2% and in NACA4412, reduces by 48.5%

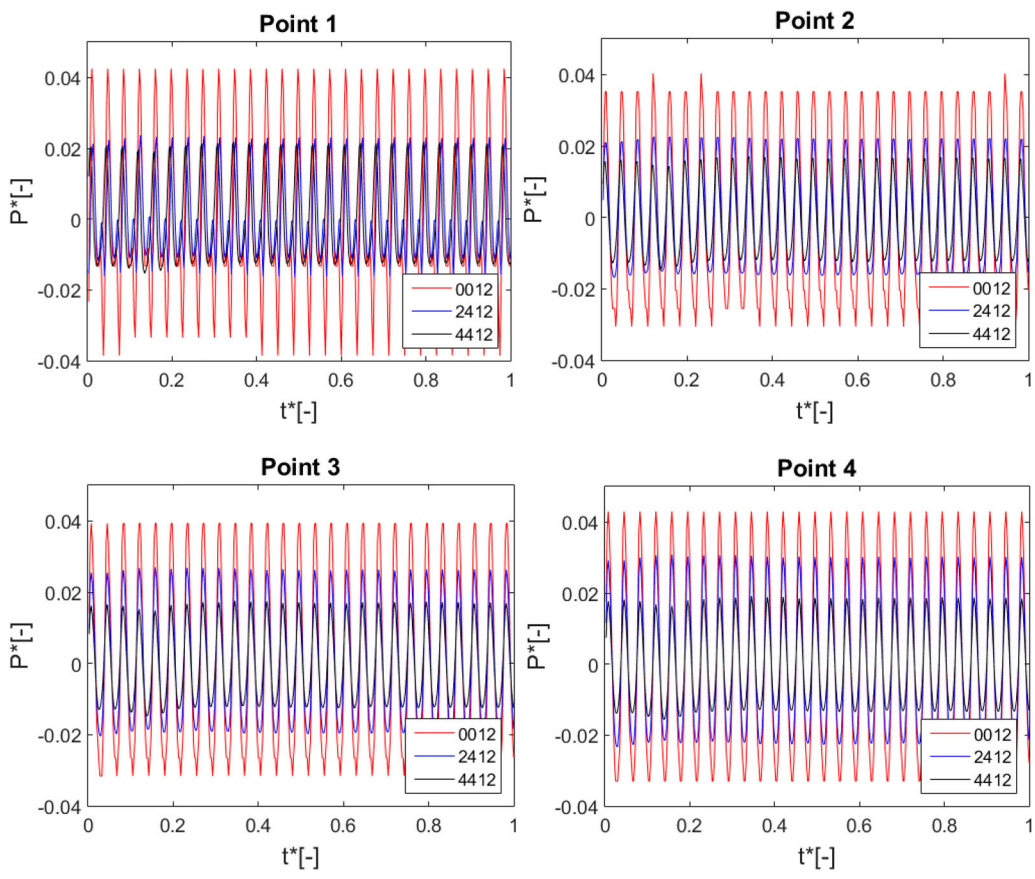

Figure 20. Instantaneous pressure fluctuations at BEP for three GV profiles.

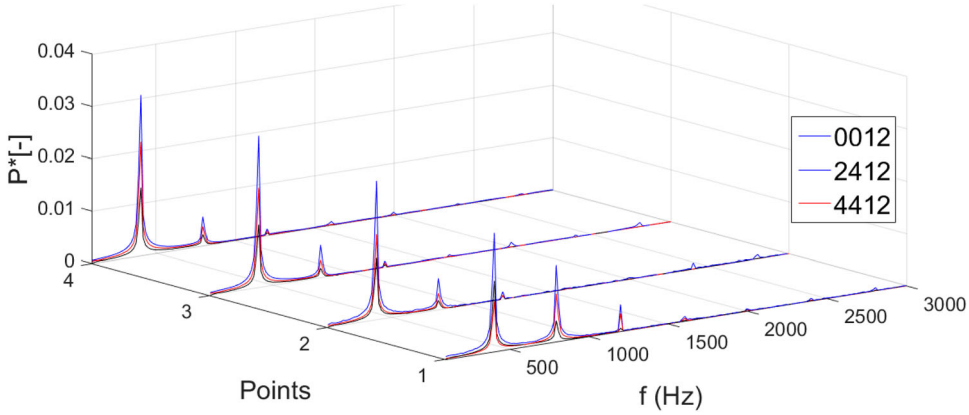

Figure 21. Frequency spectrum of the pressure–time signals of 4 points at runner inlet including GV clearance gap at BEP.

compared to NACA0012. At Point 2, the maximum pressure amplitude in NACA2412 and NACA4412 reduces by 43.8% and 57.5% respectively. At Point 3, the reduced amplitudes are 31.2% and 55.2% respectively, and 28.1% and 55.4% at Point 4 respectively.

5.5. Leakage flow at all operating conditions

Figure 17 showed the trend of V_y along the GV camber line at one operating condition. The same plot can be used to investigate the V_y at different GV opening angles. Alternatively, Leakage Flow Factor (L_{ff}) can be defined to investigate the average leakage flow along the camber line (Chitrakar, Thapa, et al., 2017). This makes it possible to observe the effect in all operating conditions using one plot. L_{ff} is defined with the following equation:

$$L_{ff} = \frac{\sum_{i=(X_1,Y_1)}^{(X_2,Y_2)} |V_{y'_i}|}{n.|V_o|} \tag{6}$$

This factor averages the V_y values by considering negative leakage flow. In Figure 22, $L_{ff}.V_o$ is plotted against the flow percentage. The flow of 100% implies BEP, lower than 100% implies part load and higher than 100% implies full load conditions. At BEP, L_{ff} in NACA4412 reduces by more than 3 times compared to NACA0012. At part load conditions, when the GV is closing, L_{ff} increases for all the cases. This is due to an increase in the pressure difference between adjacent sides of GVs at closing. NACA4412 maintains minimum L_{ff} at all the part load conditions compared to other profiles. The difference in L_{ff} between NACA0012 and NACA2412 is marginal at part load and BEP conditions.

At full load conditions, L_{ff} in NACA4412 increases gradually. This growth is representing some negative leakage flow occurring through the gap. The negative values are not shown in the graph because of the absolute terms used in the equation. At the flow percent higher than 110%, the leakage flow in NACA4412 grows bigger than in NACA0012, reaching more than 30% of the reference case. Some negative leakage in NACA2412 is also seen towards higher GV opening, but total L_{ff} remains less than other profiles. It can be seen that the L_{ff} in NACA2412 can be reduced up to 2 times compared to NACA0012 at full load conditions.

Turbines operate at high GV openings during wet seasons. This is the time when the concentration of sediment in the flow is maximum. This implies that turbines are most vulnerable to erosion in the wet season. Furthermore, due to high discharge, the flow is accompanied with higher turbulences than that in the dry season. In Figure 22, it can be seen how the vortices travel at full load conditions in NACA4412. The figure represents vorticity plot with swirling strength of 1500 Hz. The vortex starts to originate from leading edge of GV, and because of the negative leakage flow, the vortex tends to hit adjacent GV rather than going into the runner. However, due to (i) larger distance between GV's leading edge and the neighboring GV than between GV's trailing edge and the runner inlet, and (ii) lower intensity of these vortices compared to the one going into the runner for symmetrical profiles, the vortices seem to dissipate before hitting the succeeding GV. Some abrasive erosion might be seen towards the leading edge inside the gap, but the intensity of the abrasive erosion in full load operation is less because of the low pressure difference between the adjacent sides and low V_y (shown in Figure 17).

Figure 23 shows the pressure pulsation from the rotor-stator interaction (RSI) at the inlet of the runner for off-design conditions. Similar to Figure 21, the frequencies correspond to harmonics of blade passing frequency. The overall amplitude of the pressure in full load condition is higher than in part load and BEP. This is because more power is extracted when the flow is maximum. Comparing the three profiles, the amplitude of the pressure in all the points and at all the frequencies is found to

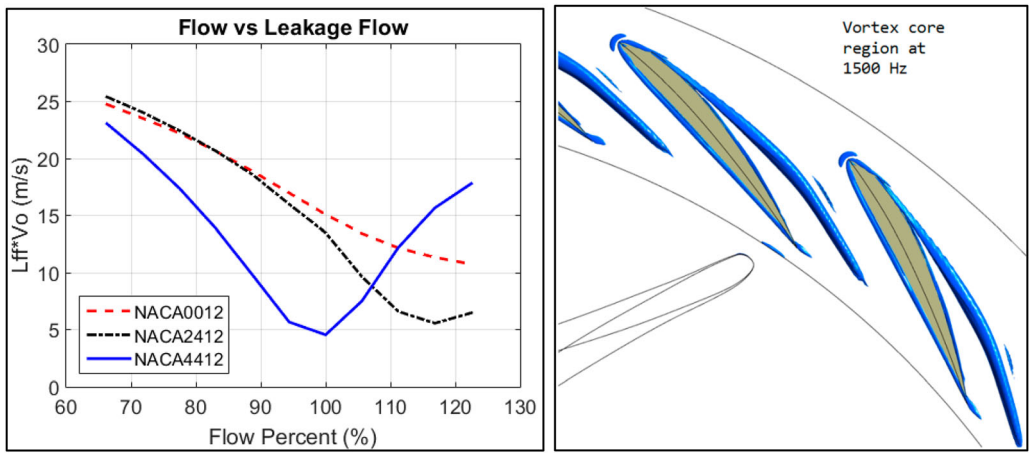

Figure 22. Leakage flow factor at all operating points and nature of leakage flow in NACA4412 at full load operations.

be maximum in NACA0012. At point 1, the maximum pressure amplitude in NACA2412 reduces by 38% compared to NACA0012 and in NACA4412, reduces by 63% at+5° GV opening angle. Similarly, the reduction of the pressure amplitude is 30% and 49% respectively at −5° GV opening angle. From Figures 15, 22 and 23, it can be inferred that despite the negative leakage flow at full load conditions in NACA4412, the resulting vortices from

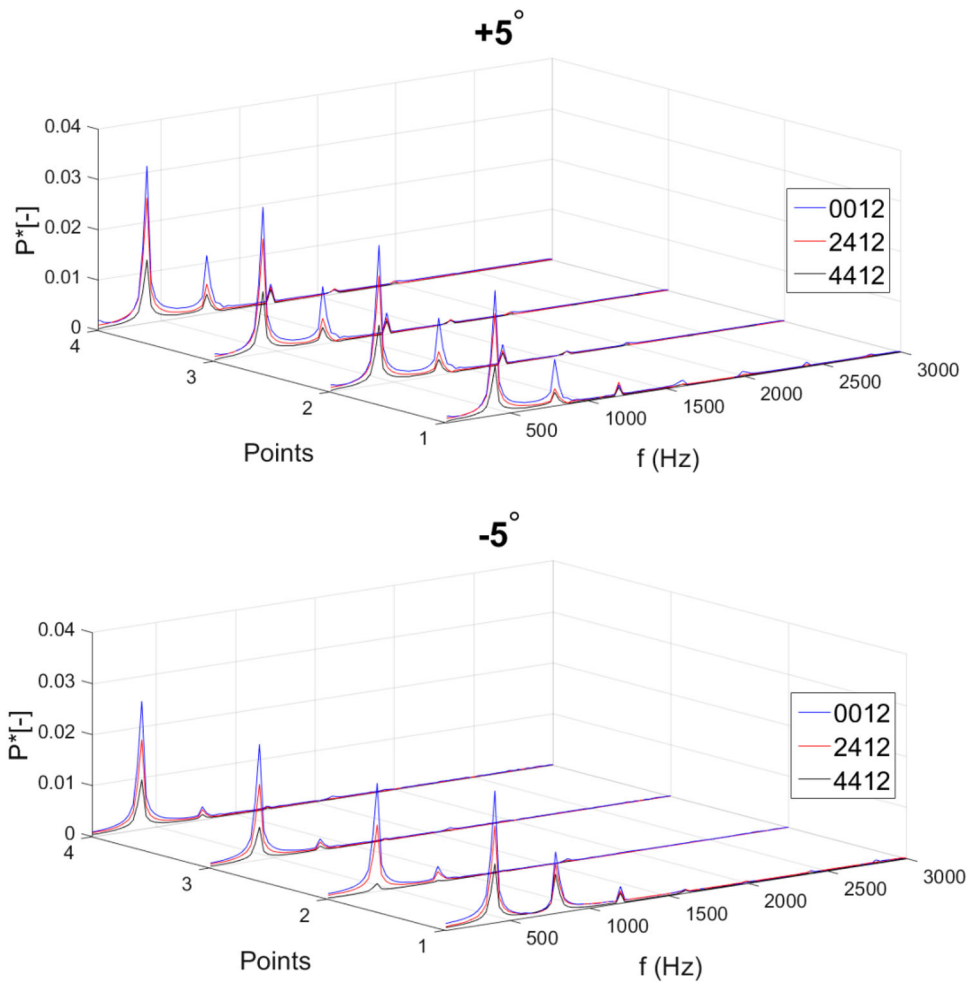

Figure 23. Pressure pulsation at runner inlet including the clearance gap at full load and part load conditions.

the GV have minimal or no influence on the efficiency of the runner and pressure pulsation downstream of the GV.

6. Conclusion

Continuous Abrasion due to sediment inside the clearance gap of the GVs increases the size of the gap. This deteriorates the main flow, adding to the total losses of the turbine and erosion of the runner blade towards inlet. On investigating the nature of the vortices originated from the leakage flow and erosion pattern of the actual runner, it was found that the vortices are responsible for erosion towards the edges of the runner blade's inlet. For a clearance gap of 2 mm, the GV containing NACA0012 profile showed reduction in the stagnation angle (α) by up to 30% near hub and shroud.

It was seen that the pressure difference between adjacent sides of the GV could be reduced by using NACA4412 profile for part load and best efficiency operation. The quantification of the leakage flow through the clearance gap was done by calculating velocity component perpendicular to the chord of the GV (V_y) and Leakage flow factor (L_{ff}). It was studied that the value of V_y along the chord reduces by up to 20% in NACA2412 and up to 40% in NACA4412 compared to NACA0012 at BEP. The efficiency of the runner was found to be increased by 1.5–3% at all the operating conditions by using NACA4412 GV profiles.

At full load operations, some negative leakage flow was seen in asymmetric profiles, which has a tendency of hitting adjacent GVs rather than flowing into the runner. However, due to lower intensity of these vortices compared to the ones in part load conditions, the vortices were seen to dissipate before striking the neighboring GV. The amplitude of the pressure pulsation at the inlet of the runner, using NACA4412 reduced to up to 57% at BEP, up to 63% at +5° and up to 49% at −5° GV opening angle, compared to NACA0012.

It can be concluded from these findings that NACA0012, which is the current GV profile at Jhimruk HPP, is not a suitable hydrofoil, as it reduces the performance of the turbine. In such sediment affected power plants, the flow downstream of the GV is aggravated due to the leakage flow through the clearance gap. On the other hand, the asymmetrical profiles studied in this paper showed improved performances in terms of erosion, efficiency as well as pressure pulsations of the runner. By using non-uniform clearance gaps in the analyses, the effect of the leakage flow on the runner can be studied more accurately. Moreover, the most optimum design of the GV can also be investigated using rigorous optimization techniques.

Acknowledgement

This study was performed as a part of a joint Ph.D. between Kathmandu University and Norwegian University of Science and Technology. This work was supported by Norwegian Research Council and Norwegian Hydropower Center.

Disclosure statement

No potential conflict of interest was reported by the authors.

References

Brekke, H. (1988). *The influence from the guide vane clearance gap on efficiency and scale effect for Francis turbines*. 14th International IAHR Symposium, Section on hydraulic machinery equipment and cavitation, Trondheim.

Brekke, H. (2002). Design of hydraulic machinery working in sand laden water. In *Abrasive erosion and corrosion of hydraulic machinery* (pp. 155–233). London: Imperial College Press.

Celik, I., Ghia, U., Roache, P., Freitas, C., Coleman, H., & Raad, P. (2008). Procedure for estimation and reporting of uncertainty due to discretization in CFD applications. *Journal of Fluids Engineering*, *130*, 078001.

Chitrakar, S., Neopane, H.P., & Dahlhaug, O.G. (2017). Particle image velocimetry investigation of the leakage flow through clearance gaps in cambered hydrofoils. *Journal of Fluids Engineering*, *139*, 091201.

Chitrakar, S., Neopane, H. P., & Dahlhaug, O.G. (2018). A review on sediment erosion challenges in hydraulic turbines. In A. Amini (Ed.), *Sedimentation engineering*. London: IntechOpen.

Chitrakar, S., Thapa, B.S., Dahlhaug, O.G., & Neopane, H.P. (2017). Numerical and experimental study of the leakage flow in guide vanes with different hydrofoils. *Journal of Computational Design and Engineering*, *4*(3), 218–230.

Chitrakar, S., Thapa, B. S., Dahlhaug, O. G., & Neopane, H. P. (2016). Numerical investigation of the flow phenomena around a low specific speed Francis turbine's guide vane cascade. *IOP Conference Series: Earth and Environmental Science*, *49*, 062016.

Dahlhaug, O., Skåre, P., Mossing, V., & Gutierrez, A. (2010). Erosion resistant coatings for Francis runners and guide-vanes. *International Journal on Hydropower and Dams*, *17*(2), 109–112.

Durbin, P., & Reif, B. (2001). *Statistical theory and modeling for turbulent flows*. Chichester: John Wiley.

Eide, S. (2004). *Numerical analysis of the head covers deflection and the leakage flow in the guide vanes of high head Francis turbines* (PhD thesis). Trondheim: Norwegian University of Science and Technology.

Felix, D., Albayrak, I., Abgottspon, A., & Boes, R. (2016). Hydro-abrasive erosion of hydraulic turbines caused by sediment – a century of research and development. *IOP Conference Series: Earth and Environmental Science*, *49*, 12001.

Fotovatikhah, F., Herrera, M., Shamshirband, S., Chau, K., Ardabili, S. F., & Piran, M. J. (2018). Survey of computational intelligence as basis to big flood management: Challenges, research directions and future work. *Engineering Applications of Computational Fluid Mechanics*, *12*(1), 411–437.

Koirala, R., Thapa, B., Neopane, H., Zhu, B., & Chhetry, B. (2016). Sediment erosion in guide vanes of Francis turbine: A case study of Kaligandaki hydropower plant. *Wear*, *362-363*, 53–60.

Koirala, R., Zhu, B., & Neopane, H. P. (2016). Effect of guide vane clearance gap on Francis turbine performance. *Energies*, *9*(275), 1–14.

Lewis, B. J., & Cimbala, J. M. (2015). Unsteady computational fluid dynamic analysis of the behavior of guide vane trailing-edge injection and its effects on downstream rotor performance in a Francis hydroturbine. *Journal of Turbomachinery*, *137*, 081001.

Masoodi, J., & Harmain, G. (2017). Sediment erosion Francis turbine runners in the Himalayan region of India. *International Journal on Hydropower and Dams*, *1*(1), 82–89.

Milliman, J., & Meade, R. (1983). World-wide delivery of river sediment to the oceans. *The Journal of Geology*, *91*(1), 1–21.

Mou, B., He, B., Zhao, D., & Chau, K. (2017). Numerical simulation of the effects of building dimensional variation on wind pressure distribution. *Engineering Applications of Computational Fluid Mechanics*, *11*(1), 293–309.

Mulu, B. G., Cervantes, M. J., Devals, C., Vu, T. C., & Guibault, F. (2015). Simulation-based investigation of unsteady flow in near-hub region of a Kaplan Turbine with experimental comparison. *Engineering Applications of Computational Fluid Mechanics*, *9*(1), 139–156.

Patel, V. A., Jain, S. V., Motwani, K. H., & Patel, R. N. (2013). Numerical optimization of guide vanes and reducer in pump running in turbine mode. *Procedia Engineering*, *51*, 797–802.

Singh, M., Banerjee, J., Patel, P., & Tiwari, H. (2013). Effect of silt erosion on Francis turbine: A case study of Maneri Bhali stage-II, Uttarakhand, India. *ISH Journal of Hydraulic Engineering*, *19*(1), 1–10.

Stachowiak, G., & Batchelor, A. (2006). *Engineering tribology*. Oxford: Elsevier.

Tallman, J., & Lakshminarayana, B. (2001). Numerical simulation of tip leakage flows in axial flow turbines, with emphasis on flow physics: Part I – effect of tip clearance height. *Journal of Turbomachinery*, *123*, 314–323.

Teran, L., Aponte, R., Munoz-Cubillos, J., Roa, C. V., Coronado, J. J., Ladino, J., . . . Rodríguez, S. A. (2016). Analysis of economic impact from erosive wear by hard particles in a run-of-the-river hydroelectric plant. *Energy*, *113*, 1188–1201.

Thapa, B. (2004). *Sand erosion in hydraulic machinery* (PhD Thesis). Trondheim: Norwegian University of Science and Technology.

Thapa, B.S., Dahlhaug, O., & Thapa, B. (2015). Sediment erosion in hydro turbines and its effect on the flow around guide vanes of Francis turbine. *Renewable and Sustainable Energy Reviews*, *49*, 1100–1113.

Thapa, B. S., Dahlhaug, O. G., & Thapa, B. (2017). Sediment erosion induced leakage flow from guide vane clearance gap in a low specific speed Francis turbine. *Renewable Energy*, *107*, 253–261.

Thapa, B.S. , Trivedi, C., & Dahlhaug, O. (2016). Design and development of guide vane cascade for a low speed number francis turbine. *Journal of Hydrodynamics*, *28*(4), 676–689.

Trivedi, C., Cervantes, M. J., & Dahlhaug, O. G. (2016). Numerical techniques applied to hydraulic turbines: A perspective review. *Applied Mechanics Reviews*, *68*, 010802.

Trivedi, C., Cervantes, M. J., & Gandhi, B. K. (2016). Investigation of a high head Francis turbine at runaway operating conditions. *Energies*, *9*(3), 149.

Vergteed, H., & Malalasekera, W. (1995). *An introduction to computational fluid dynamics*. New York, NY: John Wiley & Sons.

Wilcox, D. (1993). *Turbulence modeling for CFD*. La Canada: DCW Industries.

Zhao, W., Billdal, J. T., Nielsen, T. K., & Brekke, H. (2012). Study on the leakage flow through a clearance gap between two stationary walls. *IOP Conference Series: Earth and Environmental Science*, *15*, 022015.

Zuojun, W., Weiyang, Q., Peijie, S., Pingping, C., & Lei, Z. (2014). Tip-leakage flow loss reduction in a two-stage turbine using axisymmetric-casing contouring. *Chinese Journal of Aeronautics*, *27*(5), 1111–1121.